Supplement of The Cryosphere, 20, 1655–1677, 2026
https://doi.org/10.5194/tc-20-1655-2026-supplement

The Cryosphere Open Access EGU

Supplement of

How to model crevasse initiation? Lessons from the artificial drainage of a water-filled cavity on the Tête Rousse Glacier (Mont Blanc range, France)

Julien Brondex et al.

Correspondence to: Julien Brondex (julien.brondex@univ-grenoble-alpes.fr)

This supplement to the article "How to model crevasse initiation ? Lessons from the artificial drainage of a water-filled cavity on the Tête Rousse Glacier (Mont Blanc range, France)" describes the numerical simulations performed using linear and non-linear (Glen-Nye) viscoelastic rheologies and provides additional figures.

Additional viscoelastic simulations

We conduct a new set of viscoelastic simulations based on the experimental setup used for the diagnostic experiments presented in Section 3.3.2 of the paper. Because the unknowns of a Maxwell viscoelastic problem are displacements that accumulate over time, there is no steady-state solution to this problem, unlike in the purely viscous case, for which a steady velocity field can be computed for any given geometry. Therefore, these viscoelastic simulations are run in transient mode. Concretely, we run two sets of simulations for both the empty-cavity and cavity-free geometries: one lasting five minutes with a one-second time step, and another lasting one day with a five-minute time step. We test both a linear Maxwell viscoelastic rheology and a non-linear (Glen-Nye) Maxwell viscoelastic rheology. The equations of the model are described in Zwinger et al. (2020). Note that in the non-linear case, only the viscous component is non-linear, while the elastic part remains linear. For both rheologies, we use a Poisson's ratio of $\nu = 0.45$. We choose this value in line with, e.g., Gudmundsson (2011) or Rosier et al. (2014), because, as noted by MacAyeal et al. (2015) and discussed above, a viscoelastic model must reconcile two conflicting rheologies: the elastic rheology in which ice is considered compressible ($\nu = 0.3$), and the viscous rheology in which ice is assumed incompressible. Figures S1 and S2 show the temporal evolution of surface anomalies (i.e., the difference between the solutions obtained in the empty-cavity and no-cavity configurations) in maximum principal stress induced by the presence of an empty cavity for the linear and non-linear viscoelastic rheologies, respectively. Note that the colorbar ranges differ between the two figures.

Let us first focus on the linear case (Fig. S1). After one second of simulation, the viscoelastic solution is very close to the purely elastic one; the small differences observed in the stress pattern are entirely due to the difference in Poisson's ratio, i.e. $\nu = 0.3$ in the elastic case versus $\nu = 0.45$ in the viscoelastic case (see Fig. S3). Similarly, the differences between the patterns obtained with the viscoelastic and purely viscous solutions are mainly attributable to the assumption on ice compressibility ($\nu = 0.45$ for the viscoelastic case versus full incompressibility for the purely viscous case). As shown in Fig. S3, the fact that the stress pattern is controlled primarily by the choice of Poisson's ratio, rather than by the nature of the constitutive law, is clearly established by two additional simulations testing $\nu = 0.45$ and $\nu = 0.5$ (i.e., incompressible) for the purely elastic case, and $\nu = 0.5$ for the linear viscoelastic case. It is striking to observe how similar the diagnostic stress field computed with the purely viscous law is to those obtained with the purely elastic or viscoelastic laws when $\nu = 0.5$ (incompressible). This point is discussed in the main paper (beginning of Sections 4.1 and 5.1). Returning to Fig. S1, the stresses computed with the viscoelastic law gradually evolve toward higher tensile stresses around the cavity roof as deformations accumulate over time. The feedback of deformation on the stress field in the viscoelastic simulation is equivalent to the stress evolution that would result from an evolving geometry in the purely viscous simulation (we recall that the stress solution computed in the latter is a diagnostic stress field for the initial, undeformed geometry).

Now, let us consider the non-linear case (Fig. S2). Again, the viscoelastic solution obtained after 1 s of simulation is very close to the purely elastic one, with the small differences being attributable to the different values of Poisson's ratio. As in the linear case, the stresses computed with the non-linear viscoelastic law evolve over time toward higher tensile stresses around the cavity roof. However, this evolution is much stronger and occurs much faster than in the linear case (note again that the color scale differs between the two regimes), because it results not only from the accumulation of deformation, but also from the *progressive* feedback of strain rates on viscosity. This feedback makes the ice more fluid, leading to a concentration of stresses as discussed above. In this case, the solution obtained with the purely viscous (Glen-Nye) law more closely resembles the viscoelastic solution after several hours of simulation, rather than at the very beginning, as was observed for the linear case. As explained above, this is because, although the pure Glen-Nye solution does not account for geometric changes (we are showing the steady-state solution), it does capture the feedback of strain rate on viscosity. Moreover, while this feedback develops *progressively* in the viscoelastic case, it affects viscosity *instantaneously* in the purely viscous one. In the present case, we observe that after approximately 12 to 24 h of simulation, the viscoelastic solution has essentially converged toward the purely viscous one, with the remaining small differences in pattern again attributable to the different assumptions regarding ice compressibility (plus the fact that the Glen-Nye solution is a steady state while the viscoelastic one is transient and thus

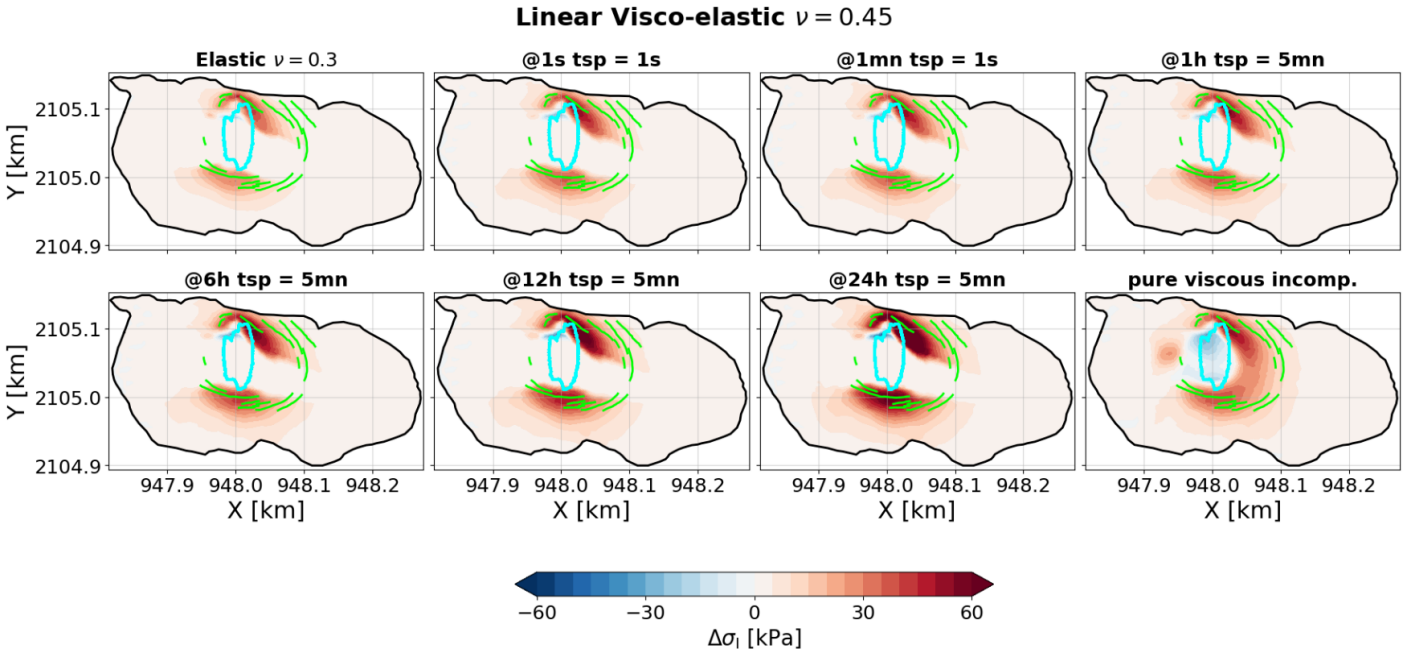

Figure S1. Temporal evolution of surface anomalies in maximum principal stress induced by the presence of an empty cavity, modeled using a linear Maxwell viscoelastic rheology with $\nu = 0.45$. The upper-left panel shows the anomaly computed assuming purely elastic behavior with $\nu = 0.3$, while the lower-right panel shows the anomaly obtained for a purely linear viscous rheology under the assumption of ice incompressibility.

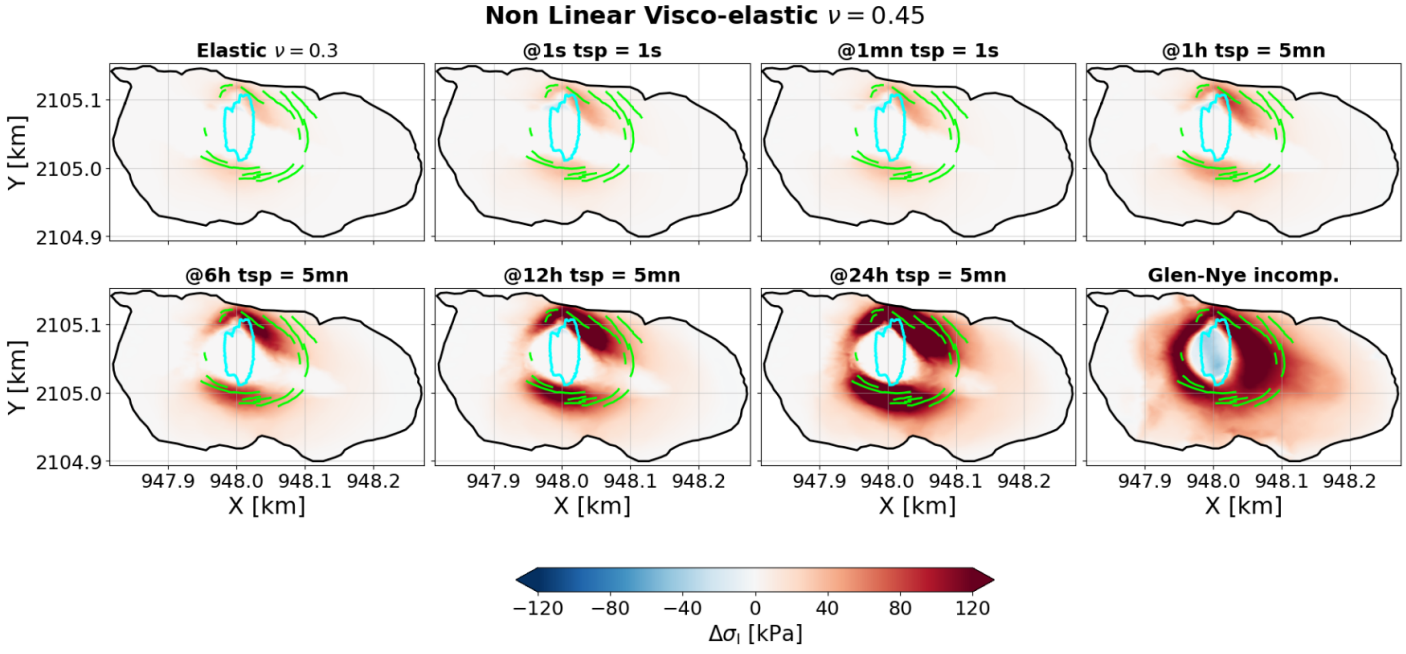

Figure S2. Same as Fig. S1, but for the non-linear (Glen-Nye) Maxwell viscoelastic rheology.

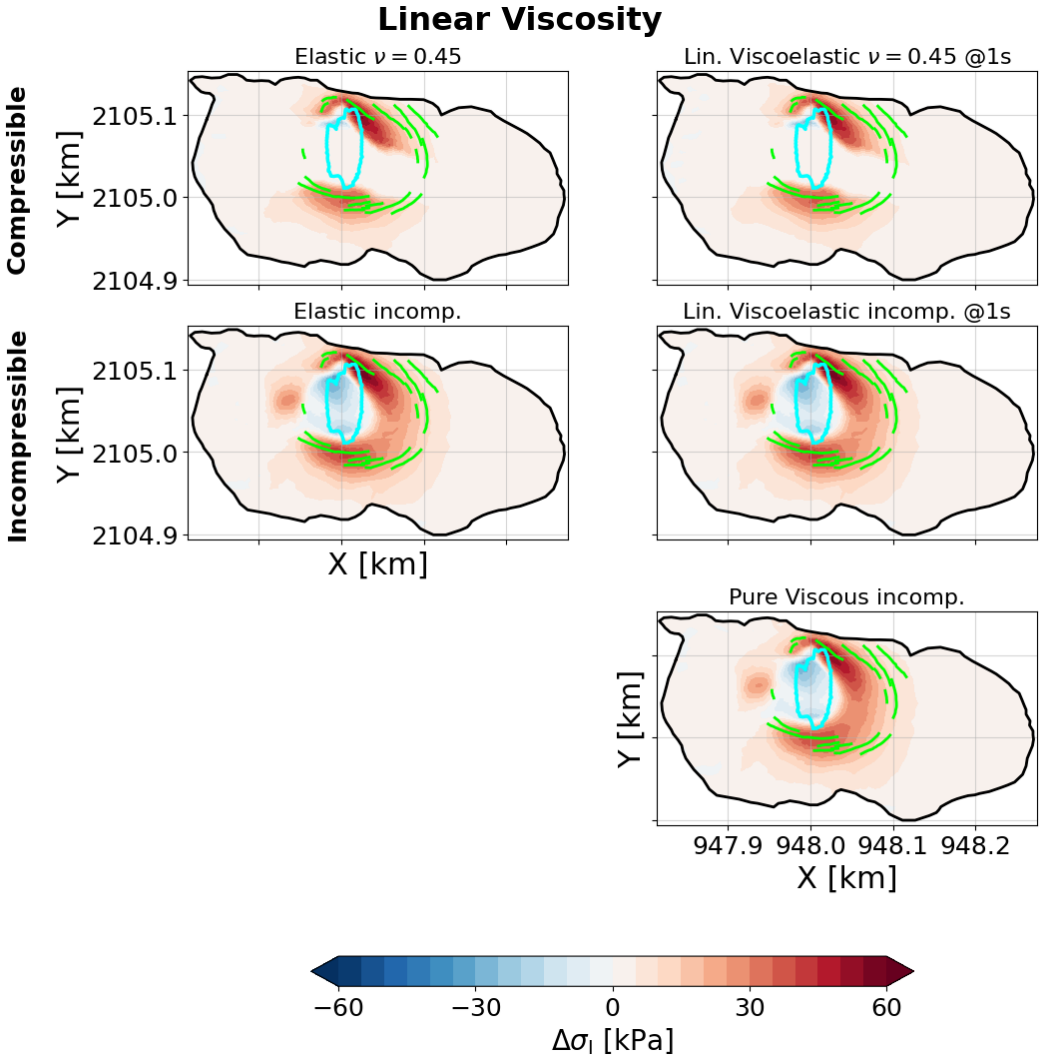

Figure S3. Surface anomalies in maximum principal stress induced by the presence of an empty cavity, modeled assuming pure elasticity with $\nu = 0.45$ (upper left), linear viscoelasticity with $\nu = 0.45$ (upper right), pure elasticity with $\nu = 0.5$ (middle left), linear viscoelasticity with $\nu = 0.5$ (middle right), and a pure linear viscous and incompressible rheology (lower right).

accumulates deformations). This result is consistent with the Maxwell time of 10 hours to 1 day in the vicinity of the cavity with $E = 1$ GPa (Fig. 8 of the main paper).

The non-linear viscoelastic simulation confirms that the solution computed using the Glen-Nye flow law represents the actual stress state in the domain, provided that sufficient time has elapsed since the perturbation for the viscous deformations (which are delayed in time) to feed back on viscosity. This characteristic timescale is the Maxwell time. Accounting for viscoelasticity would be critical only if the system was subjected to repeated perturbations at time intervals shorter than the Maxwell time. This is not the case here, and capturing the transition from the purely elastic to the purely viscous regime in response to cavity drainage is a big computationnal effort (very short time steps are required for viscoelastic simulations) that proves unnecessary for the purpose of our study. In fact, considering the purely viscous regime alone is sufficient for assessing crevasse onset in this case. These new simulations also confirm the crucial importance of accounting for the non-linear nature of ice viscosity, which leads to strong stress concentration, an effect without which the observed crevasse field cannot be explained.

Additional figures

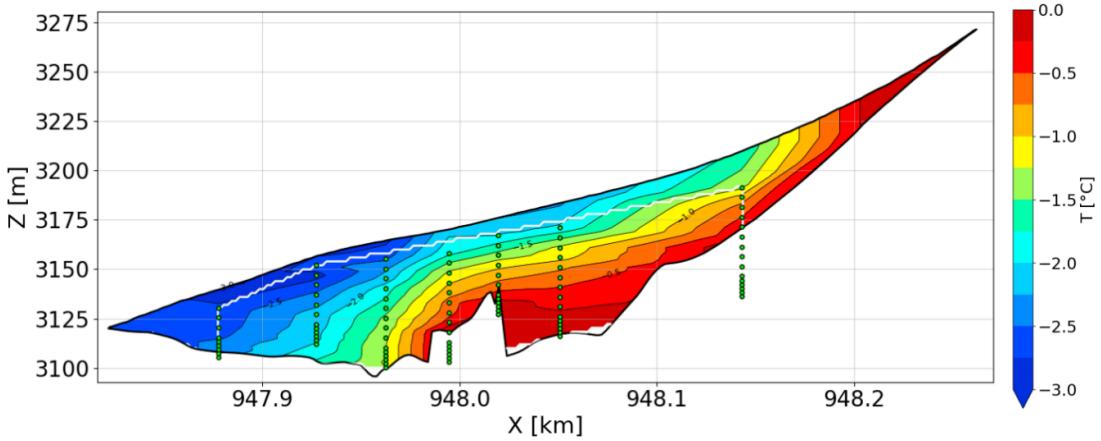

Figure S4. Reconstructed reference temperature field $T = f(x, z)$. The vertical profile is shown along the same longitudinal transect as in Fig. 8 of the main text. Temperatures are assumed uniform in the transverse direction. Green dots represent projections of thermistors used for measurements onto the cross-section. Because the boreholes are not all aligned with the selected transect (see Fig. 1a of the main text), some projected thermistors fall outside of the cross-section outline. The white solid line delineates the region where temperature is interpolated from measurements; outside this area, temperature is extrapolated from the simulation results of Gilbert et al. (2012).

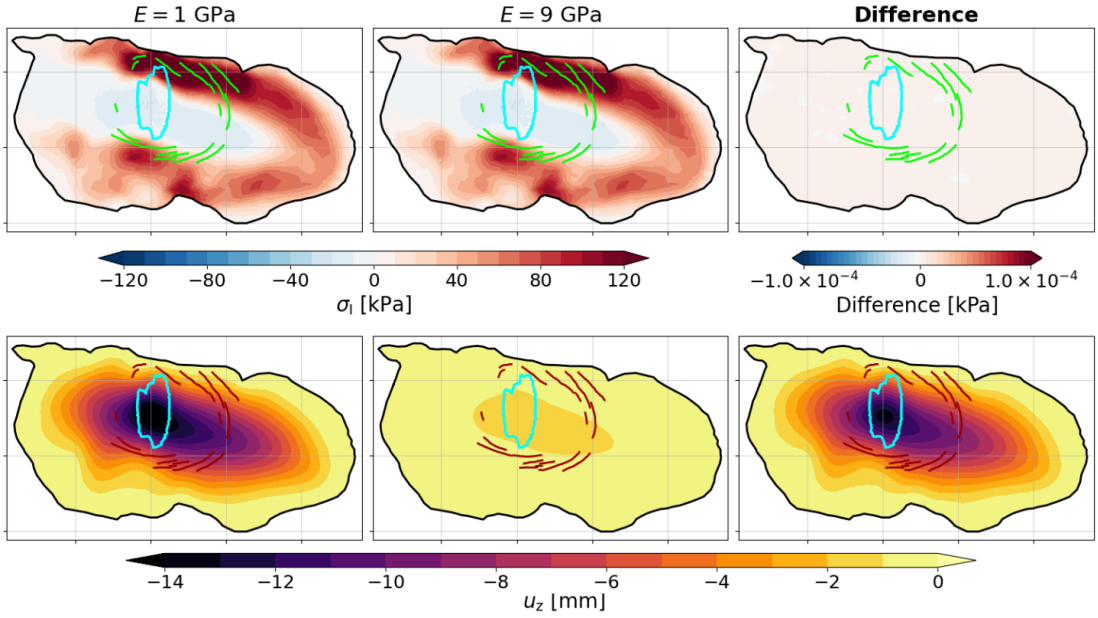

Figure S5. Absolute (first row) maximum principal stress and (second row) vertical displacement computed on the geometry with an empty cavity, using a linear elastic constitutive law with (left column) $E = 1$ GPa and (middle column) $E = 9$ GPa. The right column in each row shows the difference between the results from the two Young's modulus values. Note that a different color scale is used for stress differences (right column, top row), while the same scale is applied across all columns for displacement. Circular crevasses mapped in summer 2011 are marked in green and red in the first and second row, respectively.

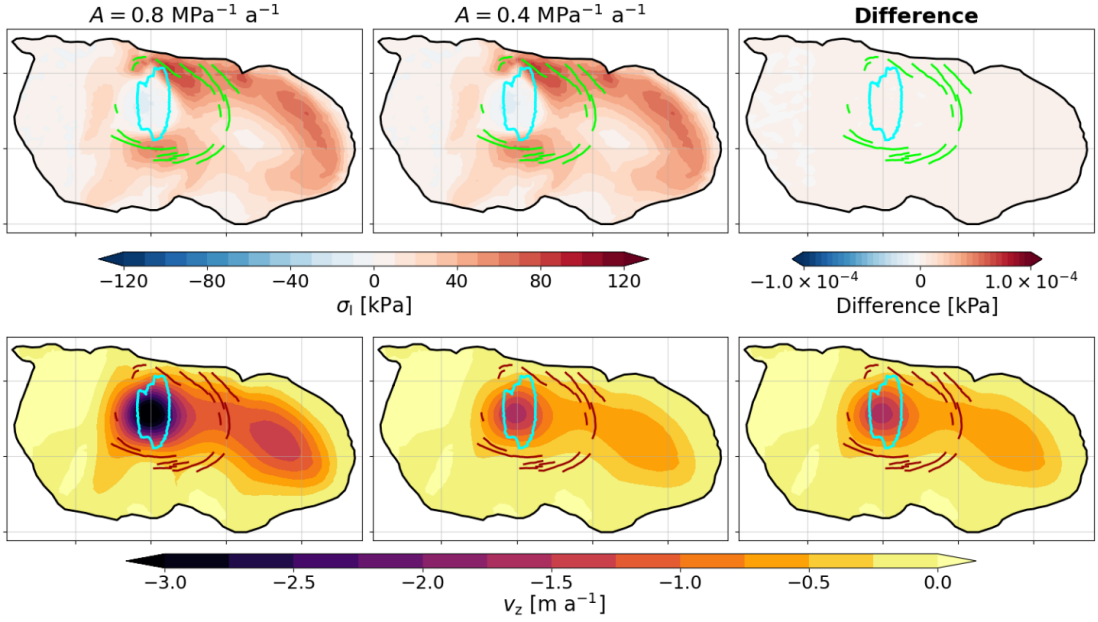

Figure S6. Same as Fig. S2, but for the linear viscous consitutive law with (left column) $A = 0.8$ MPa^{-1} a^{-1} and (middle column) $A = 0.4$ MPa^{-1} a^{-1}. The right column shows the difference between the results from the two fluidity values. Note that, in this case, the second row displays anomalies in vertical velocity rather than vertical displacement as in the elastic case.

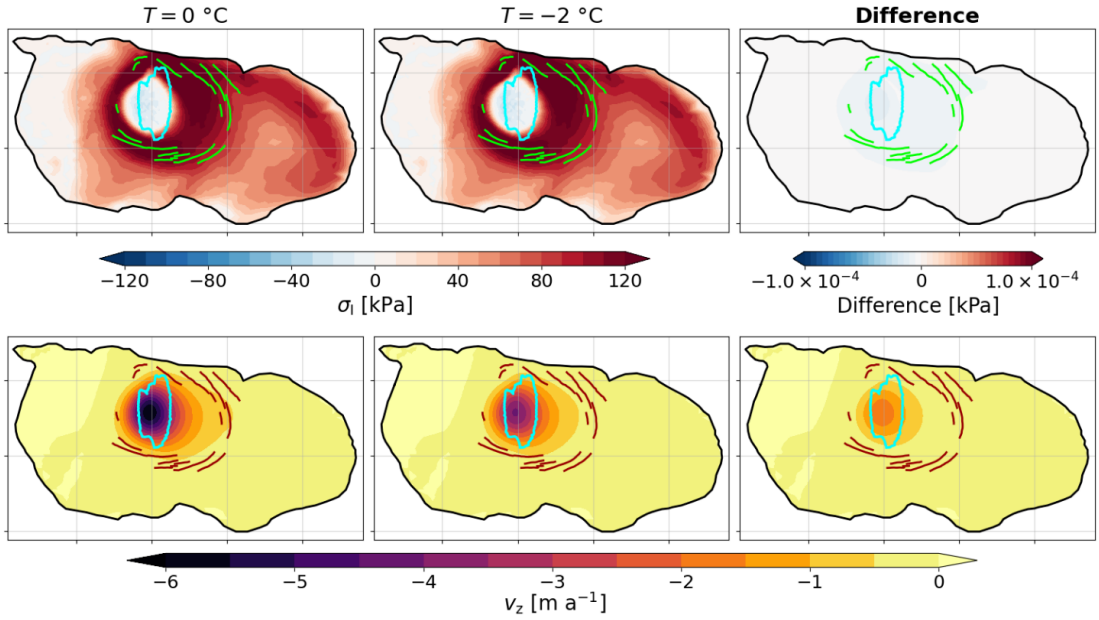

Figure S7. Same as Fig. S3, but for the non-linear Glen-Nye flow law, with a uniform temperature of (left column) $T = 0\ ^{\circ}\mathrm{C}$ and (middle column) $T = -2\ ^{\circ}\mathrm{C}$. The right column shows the difference between the results from the two temperature conditions.

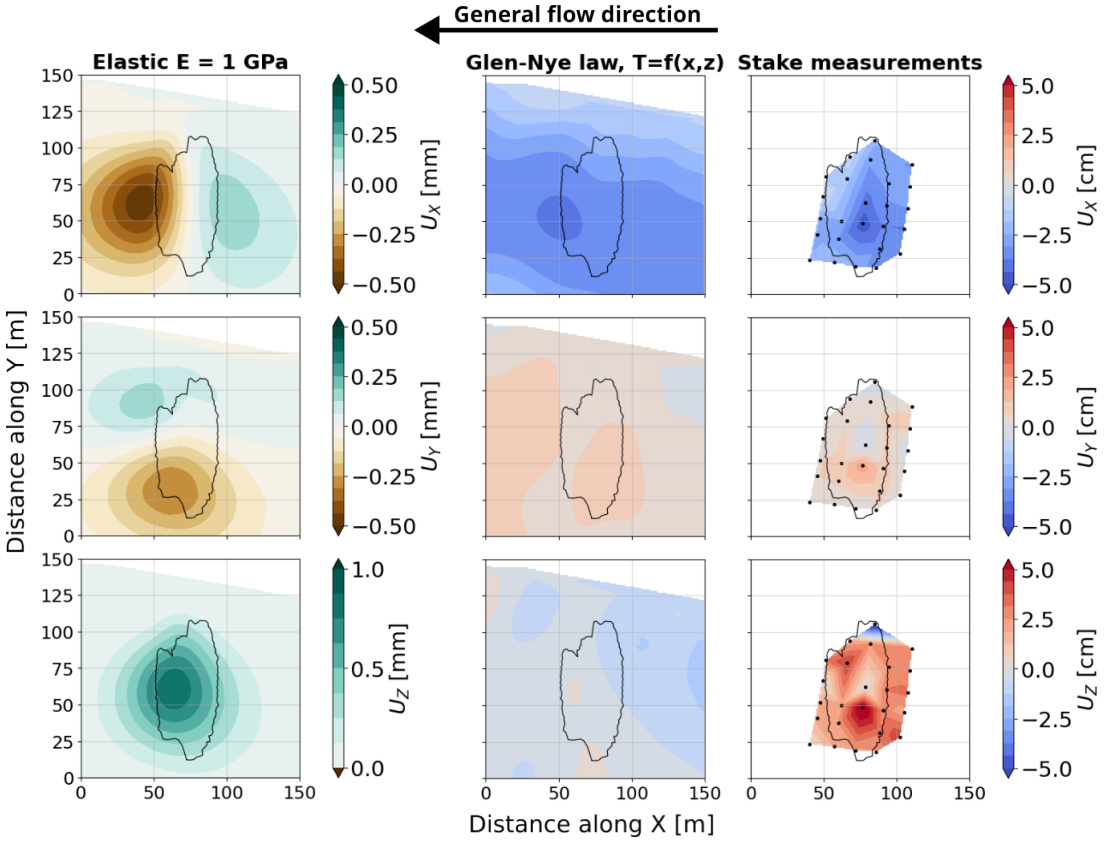

Figure S8. Total displacements in the x (top row), y (middle row) and z (bottom row) directions, obtained from (left) diagnostic simulations based on the linear elastic framework with $E = 1$ GPa, (middle) transient simulation using the Glen-Nye law with the spatially distributed T field, and (right) linearly interpolated from total station measurements at stakes between 09 September 2011 and 28 September 2011. Note that displacement units are in millimeters for the elastic case and in centimeters for the other cases. In the right column, black dots indicate positions of stakes. The cavity outline is shown in black. The general flow direction away from the cavity is indicated by the black arrow at the top of the figure.

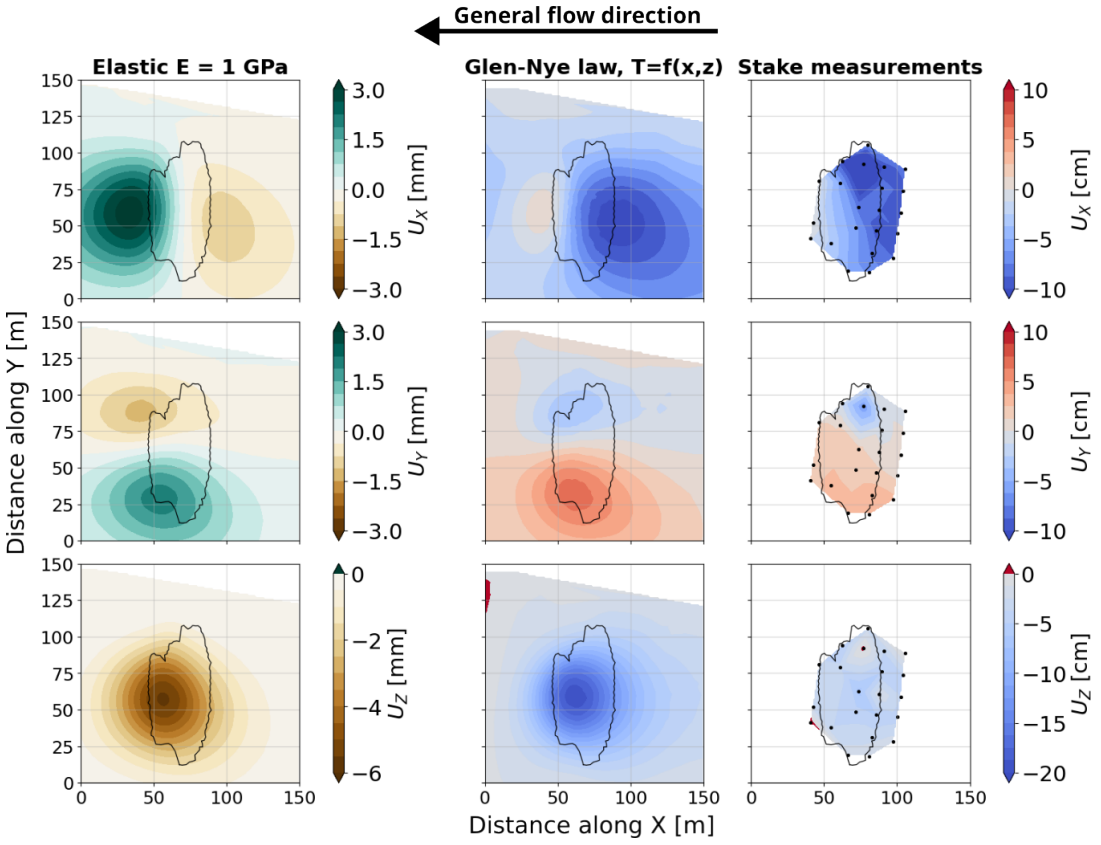

Figure S9. Same as Fig. S5, but for the period from 28 September 2011 to 21 October 2011.

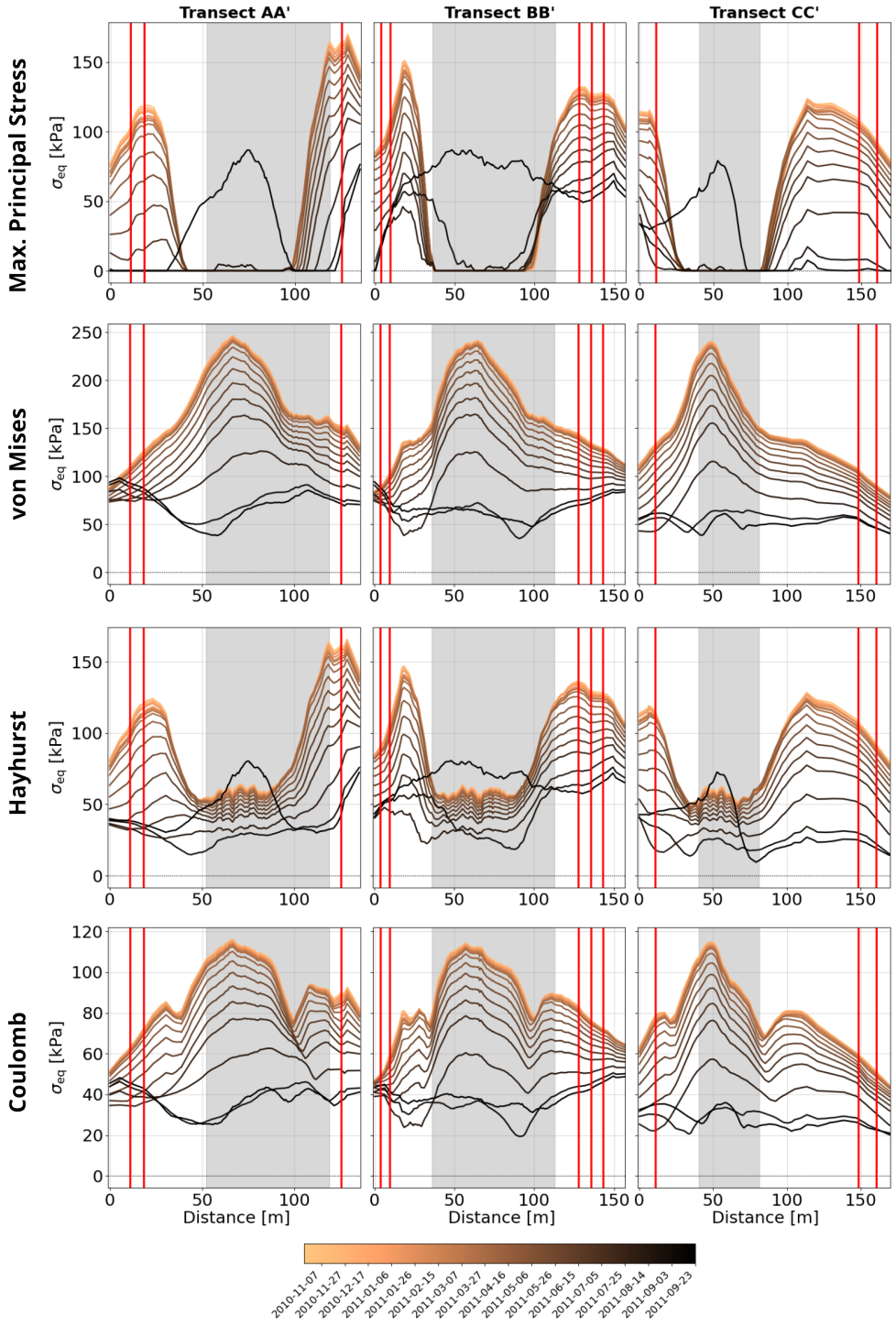

Figure S10. Evolution of surface equivalent stress along transects AA' (left column), BB' (middle column), and CC' (right column) throughout the 2010-2011 refill sequence, for the four failure criteria: MPS (first row), von Mises (second row), Hayhurst (third row), and Coulomb (last row). Transects are reported in Fig.5 of the main text (white lines). Vertical lines indicate crevasses, while the grey shaded area represents the cavity roof.

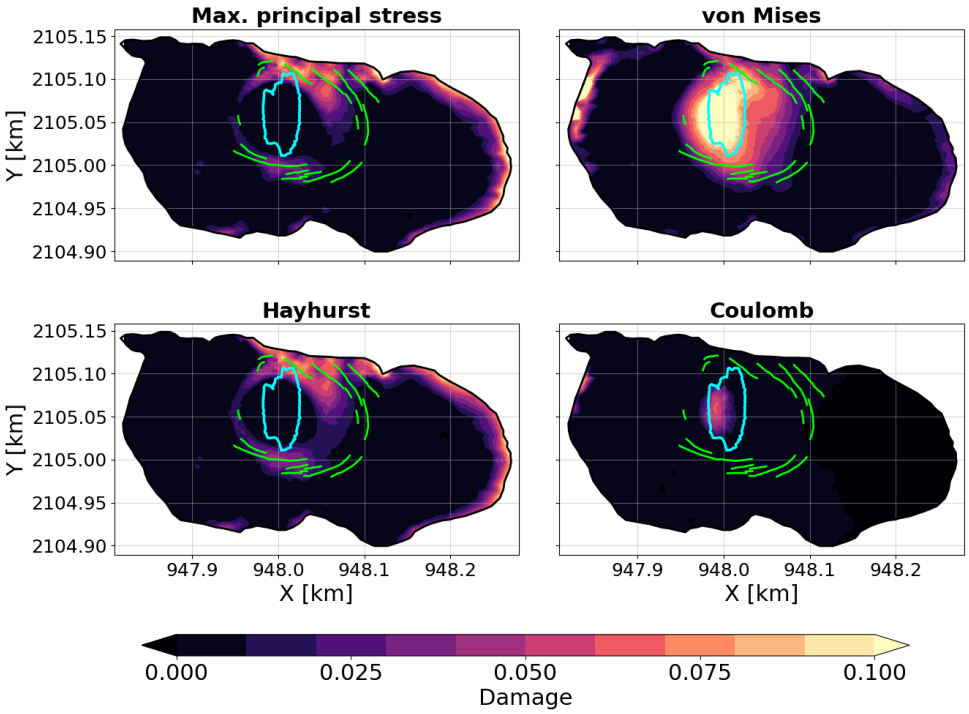

Figure S11. Damage at the surface at the end of the 2010-2011 refill sequence, computed using the four failure criteria presented in Sect. 3.2 of the main text with the combination of parameters 7 listed in Table 2 of the main text: $B = 1.72$ and $\sigma_{\mathrm{th}} = 100$ kPa. The cavity contour is shown in cyan. Circular crevasses mapped in summer 2011 are marked in green.

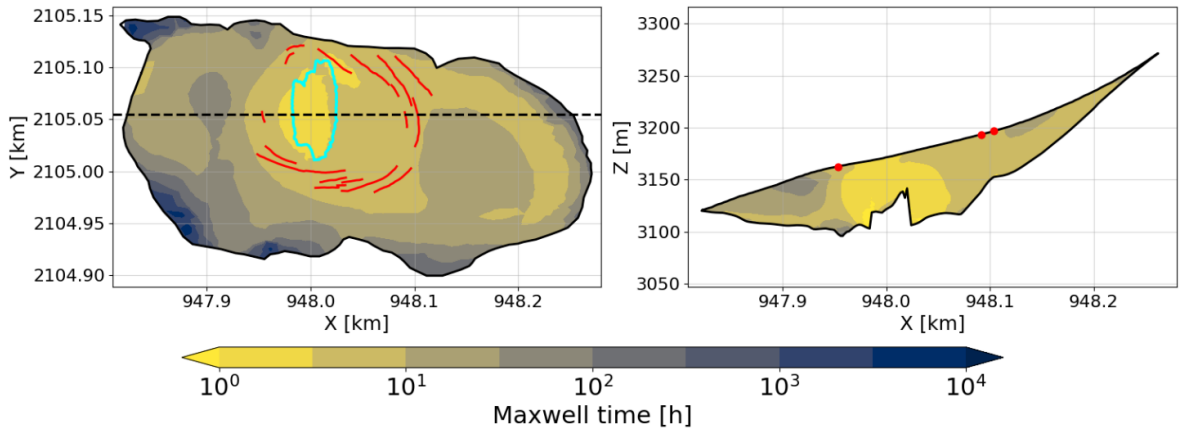

Figure S12. Maxwell time at the glacier surface (left) and across a vertical profile (right) evaluated for an empty cavity according to Eq. (6) of main text with the Glen-Nye law and for $E = 9$ GPa. The cavity contour is shown in cyan. Circular crevasses mapped in summer 2011 are marked in red. The transect along which the vertical profile is extracted is reported by the dashed black line in left panel.

References

Gilbert, A., Vincent, C., Wagnon, P., Thibert, E., and Rabatel, A.: The influence of snow cover thickness on the thermal regime of Tête Rousse Glacier (Mont Blanc range, 3200 m a.s.l.): Consequences for outburst flood hazards and glacier response to climate change, Journal of Geophysical Research: Earth Surface, 117, https://doi.org/10.1029/2011JF002258, 2012.

Gudmundsson, G. H.: Ice-stream response to ocean tides and the form of the basal sliding law, The Cryosphere, 5, 259–270, https://doi.org/10.5194/tc-5-259-2011, 2011.

MacAyeal, D. R., Sergienko, O. V., and Banwell, A. F.: A model of viscoelastic ice-shelf flexure, Journal of Glaciology, 61, 635–645, https://doi.org/10.3189/2015JoG14J169, 2015.

Rosier, S. H. R., Gudmundsson, G. H., and Green, J. A. M.: Insights into ice stream dynamics through modelling their response to tidal forcing, The Cryosphere, 8, 1763–1775, https://doi.org/10.5194/tc-8-1763-2014, 2014.

Zwinger, T., Nield, G. A., Ruokolainen, J., and King, M. A.: A new open-source viscoelastic solid earth deformation module implemented in Elmer (v8.4), Geoscientific Model Development, 13, 1155–1164, https://doi.org/10.5194/gmd-13-1155-2020, 2020.